The impact of surface morphology on the magnetovolume transition in magnetocaloric $LaFe_{11.8}Si_{1.2}$

A. Waske, E. Lovell, A. Funk, K. Sellschopp, A. Rack, L. Giebeler, P. F. Gostin, S. Fähler, and L. F. Cohen

Citation: APL Materials **4**, 106101 (2016); doi: 10.1063/1.4963840
View online: https://doi.org/10.1063/1.4963840
View Table of Contents: http://aip.scitation.org/toc/apm/4/10
Published by the American Institute of Physics

The impact of surface morphology on the magnetovolume transition in magnetocaloric $LaFe_{11.8}Si_{1.2}$

A. Waske,[1,2,a] E. Lovell,[3] A. Funk,[1,2] K. Sellschopp,[1,2] A. Rack,[4] L. Giebeler,[1] P. F. Gostin,[1,b] S. Fähler,[1] and L. F. Cohen[3]
[1]*IFW Dresden, P.O. 270116, 01171 Dresden, Germany*
[2]*Institute of Materials Science, TU Dresden, Helmholtzstr. 7, 01069 Dresden, Germany*
[3]*Blackett Laboratory, Imperial College London, SW7 2AZ London, United Kingdom*
[4]*ESRF - The European Synchrotron, CS 40220, 38043 Grenoble Cedex 9, France*

(Received 24 June 2016; accepted 19 September 2016; published online 3 October 2016)

First order magnetocaloric materials reach high entropy changes but at the same time exhibit hysteresis losses which depend on the sample's microstructure. We use non-destructive 3D X-ray microtomography to understand the role of surface morphology for the magnetovolume transition of $LaFe_{11.8}Si_{1.2}$. The technique provides unique information on the spatial distribution of the volume change at the transition and its relationship with the surface morphology. Complementary Hall probe imaging confirms that on a morphologically complex surface minimization of strain energy dominates. Our findings sketch the way for a tailored surface morphology with low hysteresis without changing the underlying phase transition.
[http://dx.doi.org/10.1063/1.4963840]

First-order magnetocaloric materials exhibit a combined magnetic and structural (or volume) phase transition at their critical temperature, which is the origin of their large magnetocaloric effect.[1] Despite favourable properties offered by second-order-type magnetocalorics,[2] like low hysteresis, highest adiabatic temperature changes can so far only be achieved by using first-order phase transition materials. Magnetocaloric $LaFe_{11.8}Si_{1.2}$ exhibits a magnetovolume transition, where the structural changes appear as an abrupt change of the lattice parameters, while its cubic crystallographic structure[3] ($Fm\bar{3}c$) is conserved. The changes in the lattice parameters lead to a volume change of the elementary cell of up to +1.5 vol. % upon cooling, depending on the Si content,[4] which can also shift the transition temperature.[5] For thermally induced transitions, the nucleation of the ferromagnetic phase starts at the surface.[6] In the literature, the magnetovolume transition of $LaFe_{11.8}Si_{1.2}$ is often studied using *in situ* X-ray diffraction because this integral technique allows a straightforward determination of the lattice constants. However, since it probes the *intrinsic* changes in the elementary cell only, it overlooks the *extrinsic* influences on the phase transition, which become dominant when moving from idealized single crystal models to functional polycrystalline materials required for application. Extrinsic features of a material, like cracks, minority phases, and structural defects, have a significant impact on the kinetics of phase transitions. For instance cracks, which appear in first-order magnetocaloric materials already after just one magnetic field or thermal cycle,[7] can pin the phase boundary and lead to a broader transition, which then typically evolves in several jumps.[8] Presence of a ferromagnetic minority phase, like α-Fe islands found in $La(Fe,Co,Si)_{13}$, has a similar pinning effect on the phase boundary.[9] Here, the energy landscape of the material is modified by these magnetic defects, slowing the transition to the ferromagnetic state. Finally, structural defects like the $Gd_5(Si_xGe_{1-x})_3$ platelets found in the matrix of first-order

[a]Author to whom correspondence should be addressed. Electronic mail: a.waske@ifw-dresden.de
[b]Current address: School of Metallurgy and Materials, University of Birmingham, Edgbaston, Birmingham B15 2TT, United Kingdom.

magnetocaloric $Gd_5Si_2Ge_2$ can seed the transition by locally inducing strain.[10] An extrinsic feature which has so far been overlooked is the shape of the sample's surface. As typical methods to examine magnetic surfaces like magneto-optical Kerr imaging or Hall probe scanning rely on flat, often polished sample surfaces, the influence of a structured surface is experimentally hard to determine. Magnetocaloric materials are typically shaped into a regenerator geometry in order to be used in a magnetocaloric device. This regenerator geometry can consist of an array of flat plates, but geometries with a non-flat surface, like packed beds[11] or 3D metal-printed structures,[12] are more beneficial in terms of heat exchange. As 2D imaging techniques have limited applicability for such structures, 3D tomographic imaging as a function of temperature is applied in this work for the first time to study the phase transition in a first-order magnetocaloric material.

$LaFe_{11.8}Si_{1.2}$ was prepared by arc melting in argon atmosphere, followed by annealing at 1373 K for 7 days under argon atmosphere in a quartz tube and subsequent water quenching. The composition of the sample was confirmed by XRD analysis and determination of the Curie temperature by a Quantum Design MPMS 5XL (not shown). The sample was crushed in a mortar and a piece with a length of approximately d = 1 mm was chosen and mounted on top of a small piece of wax. Tomographic datasets have been acquired at the beamline ID-19 (ESRF, Grenoble, France) using a pink photon energy of E = 54 keV. 2000 projection images with a pixel size of $x_{px} = 0.558$ μm have been taken at an exposure time of $t_{exp} = 0.4$ s using a thin-film single-crystal scintillator screen (10 μm-thin Eu-doped $Gd_3Ga_5O_{12}$)[13] and a magnifying optical setup (10× Olympus objective/0.3 NA). The images were captured with the ESRF in-house developed CCD camera FReloN 2k.[14] The sample temperature was monitored by an Oxford cryostream 800 with a temperature stability of $\Delta T \leq 0.1$ K. The measurements were performed upon cooling, where the image acquisition started 5 min after reaching the set temperature. The temperature was decreased to the next temperature setpoint at a rate of $\dot{T} = 5$ K/h, leading to an undershoot of just 0.02 K at each temperature step. Eleven temperature steps were taken between T = 183.6 K and T = 181.6 K at an interval of $\Delta T = 0.2$ K. The tomograms were reconstructed using standard filtered-back projection via the ESRF in-house software PyHST_2 (RAM-LAK filter).[15] The tomographic datasets have been evaluated using the Avizo® software package. First, thresholding of the datasets has been carried out using Avizo's *ISO-50* algorithm. Second, the *fill holes 3D* algorithm has been applied to the dataset in order to eliminate an imaging ring artifact in the center of the sample. For determining the volume change as a function of temperature, the number of volume elements (voxels) representing the sample has been counted for the dataset of each temperature. The volume increase ΔV is compared against the volume V of the sample measured at the highest temperature of the series (T = 183.6 K) in order to get relative values for the volume change. To correct for a temperature drift occurring with decreasing temperature, the datasets have been digitally registered (aligned) by a two-step process: First, the sample's moment of inertia tensors were rotated onto the ones of the starting dataset (T = 183.6 K). Second, the center of mass coordinates of the labeled volumes taken at the different temperatures have been translated to the center of mass coordinates of labeled volume taken at T = 183.6 K. The correction needed to compensate the thermal drift is less than 1° for rotation and between 0.8 and 2.7 μm for translation. To calculate the transformation matrix for the correction procedure, a program was written in Python using the BFGS solver of the SciPy library.[16] For determining the curvature of the sample's surface, the curvature algorithm implemented in Avizo has been employed, calculating the maximum principal curvature value at each point of a discrete triangular surface. Laboratory X-ray diffraction on powderized $LaFe_{11.8}Si_{1.2}$ in a quartz capillary was carried out using a STOE Stadi P with molybdenum $K_{\alpha 1}$ radiation in order to determine the lattice parameters of $LaFe_{11.8}Si_{1.2}$ in a wider range of temperatures from T = 122 K–293 K using an Oxford cryostream 700. The data were evaluated by the Rietveld method using Fullprof in the WinPlotR program package.[17] From these measurements, the temperature dependence of the volume change of $LaFe_{11.8}Si_{1.2}$ relative to its value at 293 K was determined. Scanning Hall probe imaging has been carried out upon cooling in 0.2 K steps in a $\mu_0 H = 1$ mT magnetic field, applied perpendicular to the sample surface, using a homemade scanning probe system in an Oxford Instruments superconducting magnet. The image window covered the central portion of the sample with a window size of 1.8×1.8 mm, and the size of one image pixel is approximately 7×7 μm^2. The Hall sensor was raster scanned vertically

moving from left to right and kept in contact with a 10 μm layer of Teflon carefully moulded to the sample surface, in order to follow the surface as closely as possible and additionally physically protect the sensor from damage. The sensor is sensitive to the field strength component in the z direction, whose Hall voltage signal has been calibrated in tesla, and during image processing the uniform 1 mT background field signal is subtracted leaving only the stray field signal from the sample. The temperature was controlled by a heater with a flow of nitrogen gas allowing a stability $\Delta T < 0.1$ K. Between each image, the set temperature was approached with an overshoot of less than 0.1 K and settled for 10 minutes before imaging. A temperature gradient due to the physical separation between the thermometer and sample position results in an absolute temperature discrepancy of up to several kelvin, the extent of which can be determined by comparison against other measurements, e.g., magnetometry. Magnetization data of the transition of the same sample on cooling confirm this discrepancy to be −4.1 K. The temperature values of the Hall imaging have been adjusted to account for this. The X-ray microtomographic scans of the Hall probe sample were carried out using a nanotom M by General Electric at an acceleration voltage of U = 125 kV, I = 100 μA, and exposure time of $t_{exp} = 0.75$ s in a voxel size of about $v_x = 2$ μm. A physical Cu filter with a thickness of about d = 300 μm was used for minimizing beam hardening artifacts. The volume reconstruction from the recorded 2-dimensional absorption images was performed with GE software dotos 2.2®. During this step, an internal software-based beam hardening and X-ray intensity fluctuation correction module was used.

In Figure 1 (left), the volume change of $LaFe_{11.8}Si_{1.2}$ as calculated from the Rietveld refinement of the XRD data (open circles) is shown together with the change of the volume of the sample in a much narrower temperature interval (full circles) as determined by counting the voxels of the tomograms at each temperature step.

The sample expansion is tracked by counting the voxels of each dataset and visualized (right side of the image) by superimposing the surface contour of the sample at different temperatures A (183.6 K), B (183.4 K), and C (181.6 K). While the volume change originating from XRD data is normalized using the room temperature value of the material, the volume increase of the tomograms is expressed relative to the first data point of the series.

As the two curves connect up very well, this proves that the volume change found by tomographic imaging in a very narrow temperature window fits to the data acquired with diffraction in a broader temperature interval. In the inset of Figure 1 (left), the volume change of the sample upon cooling as determined by X-ray microtomography is shown as a function of temperature (solid symbols). Vertical error bars originate from the determination of the threshold by the ISO-50 method, whereas horizontal error bars mark the temperature stability of the cryostream temperature controller. In the investigated narrow temperature interval, a volume increase of around 1.1 vol. % is observed upon cooling, which compares well to both the laboratory XRD results measured in a broader temperature window (cf. Figure 1 (left), open symbols) and earlier findings[7] (1.0 vol. %). The largest volume increase occurs during the first three temperature steps, i.e., between T = 183.6 K and T = 183.0 K, whereas at temperatures lower than 183 K, the volume increases very slowly.

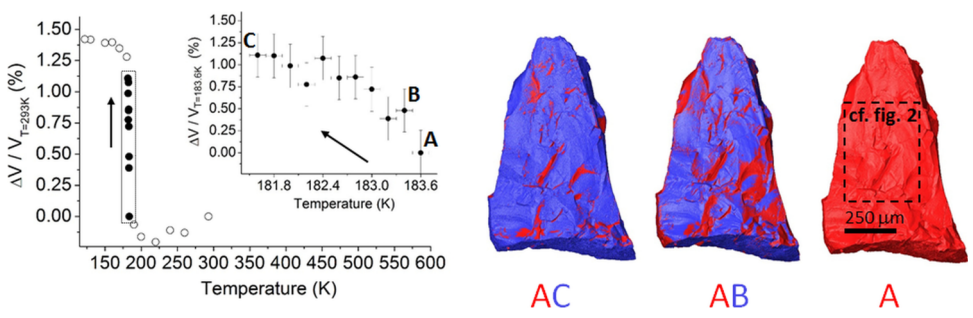

FIG. 1. Left: Volume change of $LaFe_{11.8}Si_{1.2}$ as a function of temperature upon cooling measured by X-ray diffraction and subsequent Rietveld refinement (open circles), and X-ray computed microtomography (full circles, enlarged in the inset figure). Right: Tomographic datasets taken at temperatures B and C superimposed on the one taken at temperature A.

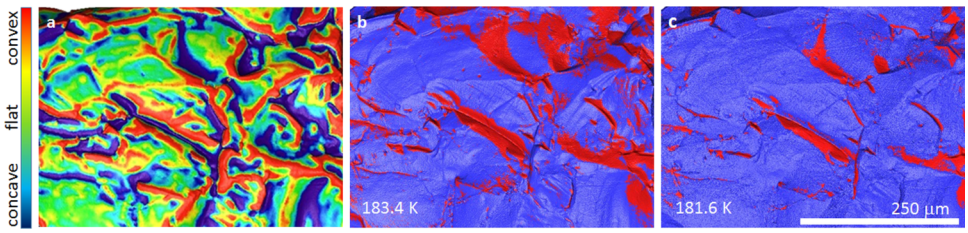

FIG. 2. (a) Curvature of a detail of the sample surface of $LaFe_{11.8}Si_{1.2}$ (shown in Fig. 1) in false color as determined from X-ray microtomographic datasets and 3D image analysis, (b) "growth" of the ferromagnetic/large phase illustrated by superposition of the sample surface at T = 183.6 K (red) and T = 183.4 K (blue), and (c) T = 181.6 K (blue).

The tracking of the volume change by 3D imaging methods allows not only for the integral determination of the changing sample volume as shown in Figure 1, but also gives spatial information on where the volume change occurs at the sample surface. To give a direct visual impression of the way the sample expands, in Figures 2(b) and 2(c), the sample's surface is shown at two temperature steps (T = 183.4 K and T = 181.6 K, both in blue) superimposed on top of the surface detected at T = 183.6 K (red). The blue regions in Figures 2(b) and 2(c) hence denote the local expansion of the sample between both temperature steps. In the following, we will compare these local expansion images with the surface curvature of the sample shown in Figure 2(a). We observe preferred nucleation and growth regions on a non-flat sample surface: the ferromagnetic phase (blue) does not grow as a homogeneous layer on the sample surface, but is restricted to certain regions of the sample. These morphological structures can easily be identified by looking at Figure 2(a), where the curvature of the surface is depicted in a false color image, in which red are convex, green are flat, and blue are concave regions of the sample surface. In particular, the nucleation of the high volume phase avoids regions with pronounced concave sample surface features, like "valleys" or troughs at the surface. This most prominent feature is evident throughout the whole temperature series, not only for the first two temperature steps (see the full video in Multimedia view). Our data suggest that the low volume phase (the paramagnetic phase) can "survive" at the bottom of the concave regions at all temperatures covered in the experiment.

The high volume phase (the ferromagnetic phase) grows very evenly on flat sample regions. The described observations are visible for all datasets with increasing volume, but they are more pronounced by taking successive temperature steps spanning the temperatures where the volume change is large.

3D X-ray computed microtomography is able to image the sample volume and some of the sample's inner features, like minority phases, pores, and cracks; it is however not sensitive to the magnetic state of the sample. In order to test our hypothesis about preferred nucleation and growth sites of the ferromagnetic phase on non-flat sample surfaces, we employed Hall probe imaging on another sample of $LaFe_{11.8}Si_{1.2}$. For the Hall probe experiment, the sample had to be reasonably flat in order to not damage the sensor, which is kept in close contact to the sample surface while it picks up the magnetic stray field from the sample along its z direction. The ferromagnetic transition is represented by a substantial increase in the stray field signal. A laboratory X-ray microtomography scan of the Hall imaging sample was taken in order to learn about the curvature of the observed surface (cf. Figure 3(a) (Multimedia view)) in a similar manner as for the synchrotron microtomography sample. Hall probe imaging with decreasing temperature reveals the way the ferromagnetic phase in $LaFe_{11.8}Si_{1.2}$ nucleates and grows ("Multimedia view"). When comparing the curvature maps of the sample surface with the Hall probe images, we can identify that the nucleation and growth are influenced by the surface morphology of the sample: (i) the ferromagnetic phase nucleates at convex regions of the samples (red areas in Figure 3(a) (Multimedia view)) like the sample edges and ridges at the sample surface, (ii) continuous growth is observed for flat regions (green/yellow), (iii) the ferromagnetic phase clearly avoids concave (blue) regions.

To conclude, our experiments show that the surface morphology has a strong influence on the magnetovolume transition in $LaFe_{11.8}Si_{1.2}$. The ferromagnetic phase prefers to nucleate in convex regions, continuously grows on flat regions, while it clearly avoids regions with strong

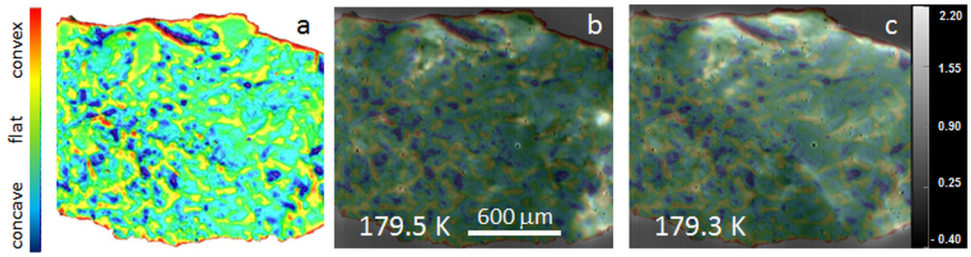

FIG. 3. (a) Curvature map of the sample used for Hall probe imaging. Overlay image of the curvature map shown on the left and a scanning Hall probe image at T = 179.5 K (b) and T = 179.3 K (c). The scale bar gives the stray field signal value perpendicular to the image window in mT units. Light areas in (b) and (c) show the ferromagnetic regions of the sample surface. (Multimedia view) [URL: http://dx.doi.org/10.1063/1.4963840.1]

concave morphology, like scratches or troughs. Local strain fields produced by a complex surface morphology can therefore lead to local T_C shifts comparable with the effect of hydrostatic pressure.[18] On the other hand, the absence of strain fields in flat regions of the sample leads to a uniform growth of the ferromagnetic phase. Hence, the surface morphology is an additional extrinsic influence on the phase transition and should be taken into account when designing magnetocaloric regenerator structures. Our experiments suggest that both the nucleation path of the magnetic transition and the hysteretic transition width in increasing and decreasing magnetic field can be influenced by the surface shape, diverting or pinning the phase boundary between para- and ferromagnetic regions. In particular we expect that the presence of convex regions existing on arbitrarily shaped samples which we find are beneficial for heterogeneous nucleation will lower the magnitude of magnetic hysteresis compared to an ideally smooth surface. Hence, tailoring the surface morphology is a promising way to control extrinsic properties like hysteresis. Indeed, recent experiments on NiMnGa thin films demonstrated that artificially introduced nucleation centers created by nano-indentation minimize the energy-costly nucleation process.[19] Moreover, as the surface is also the interface to the heat exchange liquid, a tailored morphology can be beneficial for a fast heat exchange compared to a flat surface. The results of Hall probe imaging suggest that for this temperature-driven transition, the strain field generated by the curvature of the surface dominates over the influence of the magnetic field in this very low field ($\mu_0 H$ = 1 mT) regime. For the case of a magnetic-field induced transition, competing influences of strain (favoring convex nucleation sites) and demagnetizing field (favoring concave ones) are expected. Our experiments show that X-ray microtomography data can expand the scope of 2D imaging techniques like scanning Hall imaging by providing information on the "third dimension," i.e., the sample surface morphology. Furthermore, this non-destructive technique can bring great benefits by exploring the extrinsic sample features which are relevant for the kinetics of the phase transition and the origin of hysteresis in magnetocaloric materials.

The synchrotron microtomography experiments were performed on beamline ID19 at the European Synchrotron Radiation Facility (ESRF), Grenoble, France via Proposal No. MA1739. We are grateful to Elodie Boller and Jean-Paul Valade for providing the sample environment (cryostream). A.W. and S.F. would like to gratefully acknowledge funding from the DFG SPP "Ferroic Cooling" under Grant Nos. WA3294/3-2 and FA453/11-2. L.F.C. would acknowledge European Community's 7th Framework Programme under Grant Agreement No. 310748 "DRREAM" and E.L. acknowledges EPSRC for funding.

[1] K. A. Gschneidner, Y. Mudryk, and V. K. Pecharsky, Scr. Mater. **67**(6), 572–577 (2012).
[2] K. G. Sandeman, Scr. Mater. **67**(6), 566–571 (2012).
[3] P. I. Krypiakewytsch, O. S. Zaretschniuk, E. I. Hladyschewskyj, and O. I. Bodak, Z. Anorg. Allg. Chem. **358**(1-2), 90–96 (1968).
[4] L. Jia, J. R. Sun, H. W. Zhang, F. X. Hu, C. Dong, and B. G. Shen, J. Phys.: Condens. Matter **18**(44), 9999–10007 (2006).
[5] B. G. Shen, J. R. Sun, F. X. Hu, H. W. Zhang, and Z. H. Cheng, Adv. Mater. **21**(45), 4545–4564 (2009).
[6] A. Fujita, T. Kondo, M. Kano, and H. Yako, Appl. Phys. Lett. **102**(4), 041913 (2013).
[7] A. Waske, L. Giebeler, B. Weise, A. Funk, M. Hinterstein, M. Herklotz, K. P. Skokov, S. Fähler, O. Gutfleisch, and J. Eckert, Phys. Status Solidi RRL **9**(2), 136–140 (2015).

[8] A. Bartok, M. Kustov, L. F. Cohen, A. Pasko, K. Zehani, L. Bessais, F. Mazaleyrat, and M. LoBue, J. Magn. Magn. Mater. **400**, 333–338 (2016).
[9] C. Bennati, F. Laviano, G. Durin, E. S. Olivetti, V. Basso, G. Ghigo, and M. Kuepferling, J. Magn. Magn. Mater. **400**, 339–343 (2016).
[10] J. D. Moore, K. Morrison, G. K. Perkins, D. L. Schlagel, T. A. Lograsso, K. A. Gschneidner, V. K. Pecharsky, and L. F. Cohen, Adv. Mater. **21**(37), 3780–3783 (2009).
[11] A. M. Tishin and Y. I. Spichkin, *Magnetocaloric Effect and Its Applications* (Institute of Physics Publishing, Bristol, 2003).
[12] J. D. Moore, D. Klemm, D. Lindackers, S. Grasemann, R. Träger, J. Eckert, L. Löber, S. Scudino, M. Katter, A. Barcza, K. P. Skokov, and O. Gutfleisch, J. Appl. Phys. **114**(4), 043907 (2013).
[13] P.-A. Douissard, A. Cecilia, T. Martin, V. Chevalier, M. Couchaud, T. Baumbach, K. Dupre, M. Kühbacher, and A. Rack, J. Synchrotron Rad. **17**(5), 571–583 (2010).
[14] J. C. Labiche, O. Mathon, S. Pascarelli, M. A. Newton, G. G. Ferre, C. Curfs, G. Vaughan, A. Homs, and D. F. Carreiras, Rev. Sci. Instrum. **78**, 0901301 (2007).
[15] A. Mirone, E. Brun, E. Gouillart, P. Tafforeau, and J. Kieffer, Nucl. Instrum. Methods Phys. Res., Sect. B **324**, 41–48 (2014).
[16] E. Jones, T. Oliphant, P. Peterson *et al.*, SciPy: Open Source Scientific Tools for Python, 2001-, http://www.scipy.org/.
[17] T. Roisnel and J. Rodríquez-Carvajal, Mater. Sci. Forum **378-381**, 118–123 (2001).
[18] J. Lyubina, K. Nenkov, L. Schultz, and O. Gutfleisch, Phys. Rev. Lett. **101**(17), 177203 (2008).
[19] R. Niemann, S. Hahn, A. Diestel, A. Backen, L. Schultz, K. Nielsch, M. F.-X. Wagner, and S. Fähler, APL Mater. **4**(6), 064101 (2016).